Computational Materials Science 186 (2021) 110000

Contents lists available at ScienceDirect

Computational Materials Science

journal homepage: www.elsevier.com/locate/commatsci

Single- and multi-layer arsenene as an anode material for Li, Na, and K-ion battery applications

Muammer Kanli[a], Mustafa Kurban[b], Burak Ozdemir[a], Abdullatif Onen[a], Engin Durgun[a,*]

[a] UNAM – National Nanotechnology Research Center and Institute of Materials Science and Nanotechnology, Bilkent University, Ankara 06800, Turkey
[b] Department of Electrical and Electronics Engineering, Kirsehir Ahi Evran University, 40100 Kirsehir, Turkey

A B S T R A C T

Revealing ideal electrode materials with required functionalities is a crucial step to develop high-performance alkali-ion batteries. In this study, we investigate the potential of single- (SL) and multi-layer (ML) arsenene phases (buckled and symmetric washboard) to be used as an anode material by means of *ab initio* calculations. The interaction of alkali metal atoms (*M*: Li, Na, and K) with arsenene is examined to reveal strong adatom-electrode binding and low diffusion barriers. Provided that the initial crystalline patterns are maintained, the possible *M* orderings (M_xAs) are investigated for varying ion concentrations (x). The structural deformations and the decrease in formation energy with increasing x indicate probable structural transformations. The *ab initio* molecular dynamics simulations confirm that the ordered patterns are prone to instability and crystalline to amorphous transition is induced at ambient temperature. The calculated (average) open-circuit voltages are between 0.65–0.98 V with the specific capacity range of 358–715 mAhg^{-1} for SL- and ML-M_xAs. Strong metal-electrode interaction, fast diffusion, and desired voltage range suggest arsenene as a promising anode material for alkali-ion batteries to be utilized in low charging voltage applications.

1. Introduction

Following the synthesis of ultrathin black phosphorus (phosphorene) [1,2] and fabrication of high-performance few-layer phosphorene field effect transistors [3], the class of two-dimensional (2D), monoelemental pnictogens has attracted significant interest [4]. In addition to phosphorene, single- and/or multi-layer structures of nitrogen [5], arsenic [6], antimony [7], and bismuth [8] have been realized and investigated extensively [8–14]. Their novel and diverse properties [4] suggest pnictogens as suitable materials for various technological applications including but not limited to electrochemical batteries [15–19], thermoelectric devices [20], and thin film solar cells [21].

One of the emerging areas where pnictogens can find their potential applications is the field of rechargeable alkali-ion batteries, which are crucial for portable electronics and electric vehicle industry. Therefore, the interaction of alkali metals with 2D pnictogens has been a subject of various studies [4,22–34]. In general, 2D structures supply much more accessible area than bulk materials for ion storage and diffusion, thus they are very attractive for battery applications. In this context, Li doped phosphorene has been studied and reported to have fast and directional diffusion, high average potential, and good electrical conductivity [19]. Similar characteristics have been also predicted for Na intercalated phosphoorene [18]. Sun *et al.* have shown that a hybrid system composed of few-layer phosphorene sandwiched between graphene layers exhibits a high and reversible capacity of 2440 mAhg^{-1} as a Na-ion battery electrode [35]. Accordingly, phosphorene can offer higher capacities [18,19] than graphene [36], MoS_2 [37], and Mo_2C [38], but without suitable dielectric capping. On the other hand, phosphorene has instability issues and is subject to degradation in ambient conditions [39]. Recently, antimonene has been revealed as an appealing anode material for Na-ion batteries as it enables recyclability, large-capacity (620 mAhg^{-1}), and fast electrochemical redox kinetics [16,32]. Herein, 2D pnictogen sheets [35] provide rapid ion (de)intercalation and higher power densities when compared to graphene-based electrodes, which also suffer from clustering of alkali atoms [40].

However, arsenic has been less often investigated among pnictogens [41,42], recently, Lim *et al.* [43] have synthesized arsenic and carbon nanocomposites and reported that this complex exhibits high reversible capacity in Li-ion (1306 mAhg^{-1}) and Na-ion batteries (750 mAhg^{-1}). Additionally, the interaction of alkali metals with SL buckled arsenene (SL-*hb*-As) phase has been investigated by *ab initio* methods and high storage capacities have been predicted [44]. The diffusion and voltage characteristics for Li-doped SL symmetric-washboard arsenene (SL-*sw*-As) have been also examined but for only at low concentration levels (below 20%) [45]. However, arsenene seems to be a potential anode material for alkali-ion batteries, wider concentration ranges and possible structural transformations should be explored including ML configurations of all the stable phases to reveal its full potential.

* Corresponding author.
E-mail address: durgun@unam.bilkent.edu.tr (E. Durgun).

https://doi.org/10.1016/j.commatsci.2020.110000
Received 14 June 2020; Received in revised form 4 August 2020; Accepted 10 August 2020

With this motivation, in this study, we investigate the interaction of alkali metals (*M*: Li, Na, and K) with SL and ML of arsenene phases (*hb*-As and *sw*-As). After obtaining the ground state structures, favorable adsorption sites of *M* adatoms and corresponding adsorption energies are determined. Next, the lateral diffusion and vertical intercalation barriers are calculated. Revealing the adatom adsorption, we examine alkali doped systems with varying concentrations (M_xAs, for $0 < x < 2$). *Ab initio* molecular dynamics calculations are performed to check the stability of the doped structures and also to take into account the crystal-to-amorphous structural transformation at ambient conditions. Finally, average open-circuit potentials and specific capacities are calculated for ground-state configurations and their potential to be used in alkali-ion batteries is interpreted.

2. Method

We performed first-principles calculations based density functional theory (DFT) by using Vienna ab initio simulation package (VASP) [46–49] with projector augmented wave (PAW) potentials [50,51]. The exchange-correlation interaction was described within the Perdew–-Burke–Ernzerhof (PBE) form of generalized gradient approximation (GGA) [52]. The van der Waals (vdW) correction was included by using the DFT-D3 method with Becke–Johnson damping [53,54]. A kinetic energy cutoff of 300 eV was taken for a plane-wave basis set. The numerical integrations over the Brillouin zone were calculated by using Γ-centered $24 \times 24 \times 1$ and $16 \times 12 \times 1$ *k*-points meshes [55] for SL-*hb*-As and SL-*sw*-As unit cells, respectively and then scaled accordingly for larger cells and/or ML configurations. The convergence criteria were 10^{-5} eV for electronic self-consistent field iteration and 10^{-4} eV for ionic relaxation. For monolayers, vacuum space was taken as ~20 Å to prevent interactions between periodic images. The *ab initio* molecular dynamics (AIMD) calculations were performed at 300 K implying scaled velocity approach with 1 fs time steps up to 10 ps total simulation time. Lateral and vertical diffusion barriers were obtained with nudged elastic band (NEB) technique [56,57].

The average open-circuit voltage between two different concentrations can be calculated according to the following equation [31];

$$V_M = -\frac{G(M_{x_2}\text{As}) - G(M_{x_1}\text{As}) - (x_2 - x_1)G(M)}{q(x_2 - x_1)} \quad (1)$$

where $G(M_{x_1}As)$ and $G(M_{x_2}As)$ are the Gibbs free energies of *M*-doped arsenene with successive x_1 and x_2 alkali concentrations, $G(M)$ is the Gibbs free energy of bulk alkali metal, and q is the charge state of *M* ($q = 1$). Gibbs free energy is approximated as the ground state energy since the contributions of pressure and entropy terms are not significant [58].

The specific (gravimetric) capacity is defined as;

$$C = \frac{nF}{3.6Z} \quad (2)$$

where n is the amount of the charge transfer between alkali and arsenic atoms (per mole), F is the Faraday constant, and Z is the atomic mass of arsenic (in g mol^{-1}). For theoretical capacity, the highest alkali concentration with stable configuration is considered.

The average binding energy is calculated as;

$$E_b = -\frac{E(M_x\text{As}) - E(\text{As}) - xE(M)}{x} \quad (3)$$

where $E(M_x\text{As})$ and $E(\text{As})$ are the ground state energies of alkali doped and pristine SL/ML arsenene phases, respectively. $E(M)$ is the energy of a single alkali metal atom, and x is the alkali concentration. The binding energy is also calculated with respect to total energy of bulk alkali metal and labeled as E_b'.

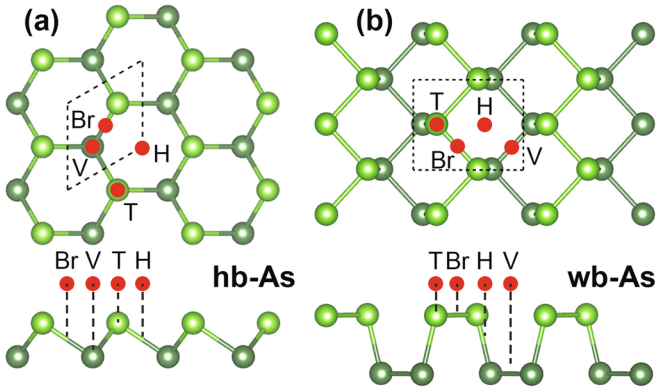

Fig. 1. Structures of (a) SL-*hb*-As and (b) SL-*sw*-As. The high symmetry adsorption sites (Bridge (Br), Valley (V), Top (T), Hollow (H)) of alkali metal atoms are shown with red dots. (For interpretation of the references to color in this figure legend, the reader is referred to the web version of this article.)

3. Results and discussion

3.1. Adatom adsorption and diffusion

We start with structural relaxation of SL-*hb*-As and SL-*sw*-As which are reported to be the stable phases of arsenene [6,12,13]. The optimized structures are shown in Fig. 1(a)–(b). The SL-*hb*-As has a hexagonal lattice similar to the layers of gray arsenic. The lattice constant ($a = b$) and As-As bond length (d_{As-As}) are calculated as 3.60 Åand 2.50 Å, respectively. On the other hand, the structure of SL-*sw*-As is similar to the layers black arsenic and has a rectangular lattice. a, b, and d_{As-As} are calculated as 3.69 Å, 4.76 Å, and 2.50 Å, respectively. The obtained structural parameters are consistent with the literature [13,59]. It should be noted that while a transition from a symmetric to asymmetric phase is predicted for the washboard antimonene and bismuthene structures, such a transition is not noticed for arsenene [59].

Following the geometry optimization, we study the interaction of alkali metal adatoms with arsenene. The possible high-symmetry adsorption sites, namely, hollow (H), top (T), valley (V), and bridge (Br), are shown in Fig. 1(a)–(b). Herein, 4×4 and 4×3 supercells are used for SL-*hb*-As and SL-*sw*-As, respectively, to minimize the $M - M$ interactions (d_{M-M} is ~15 Å). The corresponding adsorption energies (E_a) and bond lengths (d_{As-M}) for each adsorption site are given in Table 1. For SL-*hb*-As, the most favorable adsorption site is the V-site with E_a of 1.62, 1.23, and 1.49 eV for Li, Na, and K, respectively. While H- and T-sites are also found to be local minima, *M* adatoms do not stay at Br-site and shift to V-site. On the other hand, for SL-*sw*-As, H-site is found to be the most stable adsorption site with E_a of 1.81, 1.31, and 1.58 eV for Li, Na, and K, respectively. Except Li atom, Br- and H-sites are also stable adsorption spots, however adatoms initially on T-site move to H-site. When results are compared, E_a of SL-*sw*-As are slightly larger than those of SL-*hb*-As but being within the same range points out similar chemisorption characteristics. Positive E_a for all cases indicates that the adsorption is exothermic and *M* atoms favor the sites with maximum coordination number [18]. Considering the most favorable adsorption sites, Li has the strongest binding among Na and K. However, d_{As-M} follows the expected variation with the size of *M*, E_a does not regularly decrease down in alkali-group. This trend is correlated with the ionization energies of the *M* adatoms and their interactions with the substrate [30] clarifying Li > K > Na order. Bond strength of adatom over a substrate is an important parameter for battery applications [44,45,60–63]. Strong binding suggests that the migration of Li from the cathode to the anode should be more favorable than Na and K. This implies that the arsenene surfaces are more effective in attracting Li when compared to Na and K. Additionally, except Li, E_a' is positive for the most favorable sites indicating that alkali atom prefers to bind to

Table 1
The adsorption energy with respect to a single alkali atom (E_a) or bulk alkali metal (E'_a) and corresponding bonding distance between alkali atom (M) and arsenene (d_{As-M}) for high symmetry adsorption sites of SL-*hb*-As and SL-*sw*-As.

Phase	M	Br			H			T			V		
		E_a (eV)	E'_a (eV)	d_{As-M} (Å)	E_a (eV)	E'_a (eV)	d_{As-M} (Å)	E_a (eV)	E'_a (eV)	d_{As-M} (Å)	E_a (eV)	E'_a (eV)	d_{As-M} (Å)
hb-As	Li	→ V			1.54	-0.23	2.67	1.18	-0.59	2.45	1.62	-0.15	2.60
	Na	→ V			1.23	-0.01	2.99	0.98	-0.25	2.76	1.23	-0.01	2.97
	K	→ V			1.47	0.53	3.37	1.33	0.39	3.13	1.49	0.55	3.35
sw-As	Li	1.19	-0.34	2.54	1.81	0.28	2.50	→ H			→ H		
	Na	0.97	-0.20	2.91	1.31	0.14	2.88	→ H			1.24	0.07	2.85
	K	1.32	0.41	3.24	1.58	0.67	3.25	→ H			1.53	0.62	3.21

arsenene instead of forming a cluster.

While calculated E_a (1.23–1.62 eV for SL-*hb*-As and 1.31–1.81 eV for SL-*sw*-As) are higher than those for graphene [29] (0.46–1.10 eV), they are within the same range but smaller than those for phosphorene [18,19] (1.59–1.97 eV) and antimonene [15,22,32] (1.41–1.95 eV). Strong alkali-arsenene interaction can assure reversible battery operation and prevent alkali metal precipitation [60]. High adsorption ability of arsenene (especially for Li) can provide enhancement of cycling stability of battery and improve the performance of cathode.

The ion diffusion in the anode is one of the significant parameters during the charging and discharging process as it considerably influences the battery performance. Therefore, we calculate the energy barriers (ΔE) of M along possible diffusion pathways by using NEB technique and the results are shown in Fig. 2. Our results show that V – H – V and H – V – H are the fastest diffusion pathways for all M adatoms on SL-*hb*-As and SL-sw-As, respectively and ΔE(*hb*-As) is slightly smaller than ΔE(*sw*-As). For Li, ΔE are calculated as 0.11 eV and 0.12 eV, they are lower than that of black phosphorene (0.68 eV) along armchair direction [64], silicene (1.2 eV) [65], MoS_2 (0.25 eV) [66], VS_2 (0.22 eV) [66], graphene (0.33 eV) [67], germanene (0.5 eV) [65] and close to that of stanene (0.1 eV) [65]. On the other hand, they are higher than that of black phosphorene (0.08 eV) along zigzag direction [64]. For Na, ΔE are equal to 0.04 eV and 0.07 eV and are much smaller than that of silicene (3.56 eV), germanene (2.19 eV) and stanene (0.8 eV) [65]. Lastly, for K, ΔE are obtained as 0.03 eV and 0.05 eV, and are smaller than that of C_3N monolayer (0.07 eV) [68] and blue phosphorene (0.05 eV) [69]. In general, ΔE decrease from Li to K, and they are smaller than the reported diffusion barriers for various 2D systems, indicating fast diffusivity, which is a notable feature to be considered as an anode material for alkali-ion batteries.

3.2. Alkali metal doping: single-layer

In this section, we investigate M doping of SL-*hb*-As and SL-*sw*-As for varying concentrations (M_xAs). For each case, various doping sites are tested and the lowest energy configurations are determined. The optimized structures are represented in Fig. 3(a)–(b). It is revealed that the crystalline structures are preserved up to M_2As and $M_{0.5}$As for SL-*hb*-As and SL-*sw*-As, respectively. It should be noted that the highest concentration for Li/Na is smaller than the theoretical expectation [43] as only the ordered patterns are taken into consideration.

The average binding energies of alkali metals, $E_b(M)$ for varying x

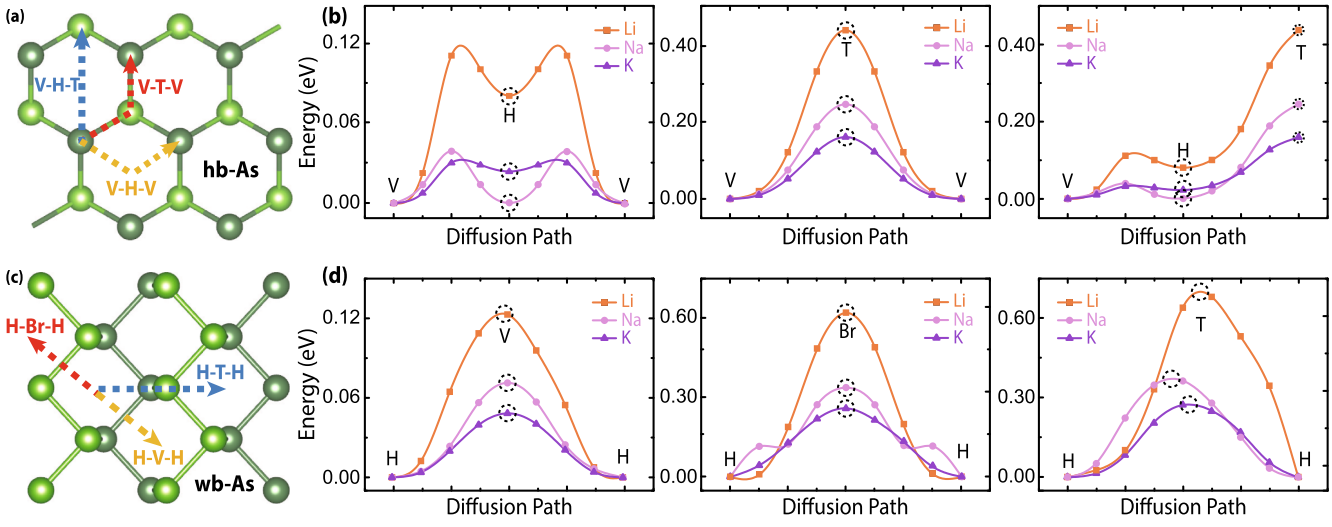

Fig. 2. Lateral diffusion pathways and the energy variation for (a),(b) SL-*hb*-As and (c),(d) SL-*sw*-As.

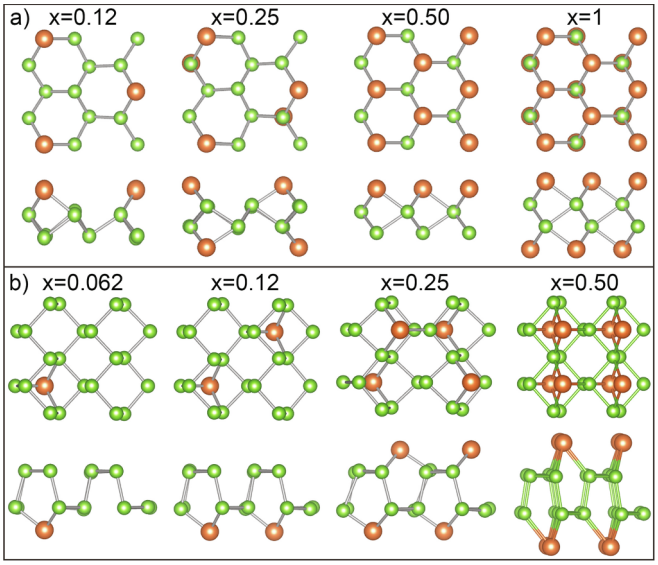

Fig. 3. The optimized structures of M-doped (a) SL-*hb*-As and (b) SL-*sw*-As, for varying M concentrations (M_xAs).

are summarized in Table 2. $E_b(Li, Na, K)$ are calculated to be in the range of 1.57–1.76 eV, 1.10–1.27 eV, and 1.05–1.20 eV for SL-*hb*-As. Similar to E_a, they are smaller than those for SL-*sw*-As, which are calculated as 1.90–1.98 eV, 1.40–1.52 eV, and 1.42–1.66 eV. For SL-*hb*-As, however, $E_b(Li, Na)$ are smaller than the corresponding $E_a(Li, Na)$ up to $x = 0.5$, they surpass it above this concentration. On the other hand, $E_b(K)$ is smaller than $E_a(K)$ for all concentrations. For SL-*sw*-As, $E_b(M)$ is (in general) larger than $E_a(M)$. However, there seems like an increase in average binding energy, this actually can be attributed to the energy lowering due to structural deformations (see below). Positive E_b' for all cases confirms that alkali atoms favor bonding to arsenene instead of cluster formation. Together with $E_b(M)$, the formation energy of M_xAs ($E_f(M)$) is calculated. For both phases, $E_f(M)$ are smaller than those of bare arsenene (3.13 eV) [59] for all M_xAs and they also decrease with increasing x. The decrease in $E_f(M)$ is due to the weakened electrostatic interaction between arsenene and M atoms and enhanced $M - M$ repulsion in ordered configurations. It should also be noted that while pristine arsenene phases are semiconducting, alkali-doped systems are metallic [44,45]. The corresponding electronic band structures for $x = 0.5$ are available as Supplemental Material [70].

Open-circuit voltage (V_M) with respect to M is an important parameter which characterizes the performance of the alkali-ion battery and shows the capacity of an anode. Assuming a standard half-cell reaction, a theoretical V_M profile can be estimated as an average voltage by using Eq. (1). V_M has been reported for alkali doped arsenene phases presuming that the crystalline structure is maintained at ambient conditions [44,45]. Although we also start with ordered configurations, deformations are noticed with increasing x, indicating a probable crystalline to amorphous transition. To reveal this issue, we perform AIMD calculations at 300 K up to 10 ps for SL-*hb*-As. This phase is considered as a prototype since its storage capacity is higher than that of SL-*sw*-As. Following the AIMD steps, the total energy of the system is significantly lowered, the crystallinity is altered, and an amorphous-like (unordered) structure is obtained. The revised V_M with respect to the total energy of amorphous structures for varying x and also for specific capacity (C) is shown in Fig. 4. However, the calculated V_M values are lower than the estimated data for crystalline phases, they are comparable with the experimental results [43]. The $V(M)$ reach up to a maximum of 0.88, 0.68, and 0.72 V for Li, Na, and K, respectively, and follow a sequence of $V_{Li} > V_{Na} > V_K$. The variation of voltage depends not only on the M type but also on the anode material. For instance, the trends in graphite and boron doped graphite (BC_3) are $V_K > V_{Li}$ (Na does not even intercalate graphite) [71] and $V_K > V_{Na} > V_{Li}$ [72], respectively. Moreover, the experimental voltage order of bulk arsenic [43] is measured as $V_{Li} > V_{Na}$, which agrees with our results. Different from crystalline phases, V_M rise up to $x = 1$ for Li, and $x = 0.5$ for Na and K and then starts to decrease for increasing cation content. This could be due to the fact that amorphous phase becomes more stable with doping up to a certain concentration. The $V_{Na,K}$ reduces almost to

Table 2
The average binding energies calculated with respect to single alkali atom (E_b) or bulk alkali metal (E_b') and the average bonding distance between alkali atom and arsenene (d_{As-M}) for SL-*hb*-As and SL-*sw*-As with varying M concentrations (M_xAs).

Phase	M	x	E_b (eV)	E_b' (eV)	E_f (eV)	d_{As-M}(Å)
hb-As	Li	0.12	1.58	0.00	2.98	2.57
		0.25	1.61	0.02	2.84	2.55
		0.50	1.57	-0.01	2.62	2.60
		1.00	1.76	0.17	2.45	2.60
		2.00	1.73	0.14	2.20	2.69
	Na	0.12	1.10	0.03	2.92	2.93
		0.25	1.10	0.04	2.74	2.95
		0.50	1.21	0.15	2.50	3.32
		1.00	1.27	0.20	2.21	3.17
		2.00	1.29	0.22	1.91	3.07
	K	0.12	1.20	0.38	2.93	3.27
		0.25	1.15	0.33	2.75	3.31
		0.50	1.05	0.23	2.45	3.36
		1.00	1.15	0.32	2.15	3.42
		2.00	1.07	0.25	1.76	3.47
sw-As	Li	0.062	1.93	0.33	3.11	2.50
		0.12	1.97	0.37	3.05	2.50
		0.25	1.95	0.34	2.93	2.46
		0.50	1.97	0.37	2.78	2.52
	Na	0.062	1.42	0.34	3.08	2.87
		0.12	1.51	0.42	2.99	2.86
		0.25	1.44	0.35	2.83	2.88
		0.50	1.51	0.42	2.62	2.98
	K	0.062	1.64	0.77	3.09	3.21
		0.12	1.65	0.78	3.01	3.20
		0.25	1.54	0.67	2.85	3.22
		0.50	1.41	0.54	2.59	3.30

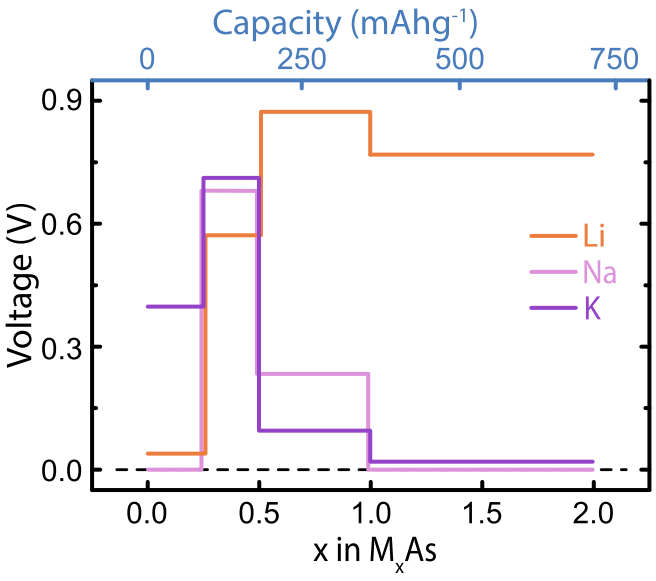

Fig. 4. Average open-circuit voltages for SL-*hb*-As coated with alkali metals (Li, Na, and K) with varying concentration (M_xAs). The optimized (amorphous) structures are obtained with *ab initio* molecular dynamics calculations performed at ambient temperature.

0 V for $x > 1$, indicating that the suggested configuration cannot occupy that amount of alkali metals. The obtained V_M are lower than Li (and Na) doped antimonene (1.22 V) [32], phosphorene (2.9 V) [19], graphite (~1.5 V) [66], TiO_2 (~1.5 V) [73], 2H-MoS_2 (1.25 V) [74] and 1H-VS_2 (1.30 V). It should be noted that the desired potential range is between 0.1–1 V for anode materials [75]. Additionally, the corresponding (maximum) theoretical specific capacity (C) is 715 mAhg^{-1} and 358 mAhg^{-1} for Li and Na/K, respectively. Thus, M_xAs with a high C can be a promising candidate for low charging voltage applications.

3.3. Alkali metal doping: multi-layer

Next, we study the M-doped multilayer (periodic) arsenene phases (ML-*hb*-As and ML-*sw*-As) for varying concentrations (M_xAs). We start by analyzing Li intercalation through arsenene layers. Li has been chosen as an exemplary, since it has the smallest radius and the calculated energy barriers (ΔE) can set the lowest limit. The intercalation paths and the energy variation are shown in Fig. 5. ΔE are calculated as

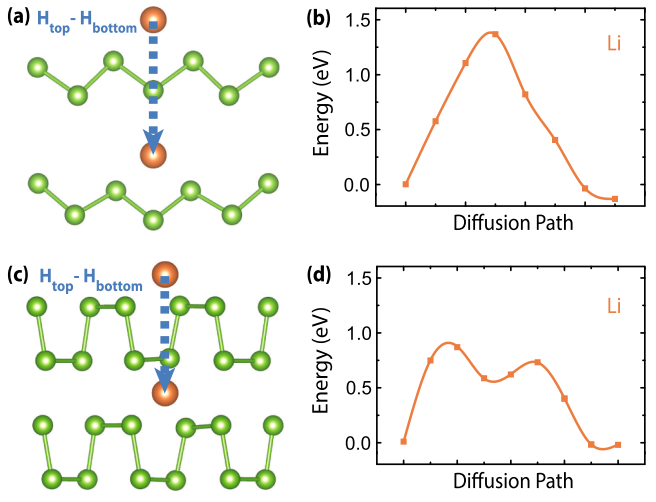

Fig. 5. Vertical diffusion pathways and the energy variation for intercalation of Li in (a)-(b) ML-*hb*-As and (c)-(d) ML-*sw*-As.

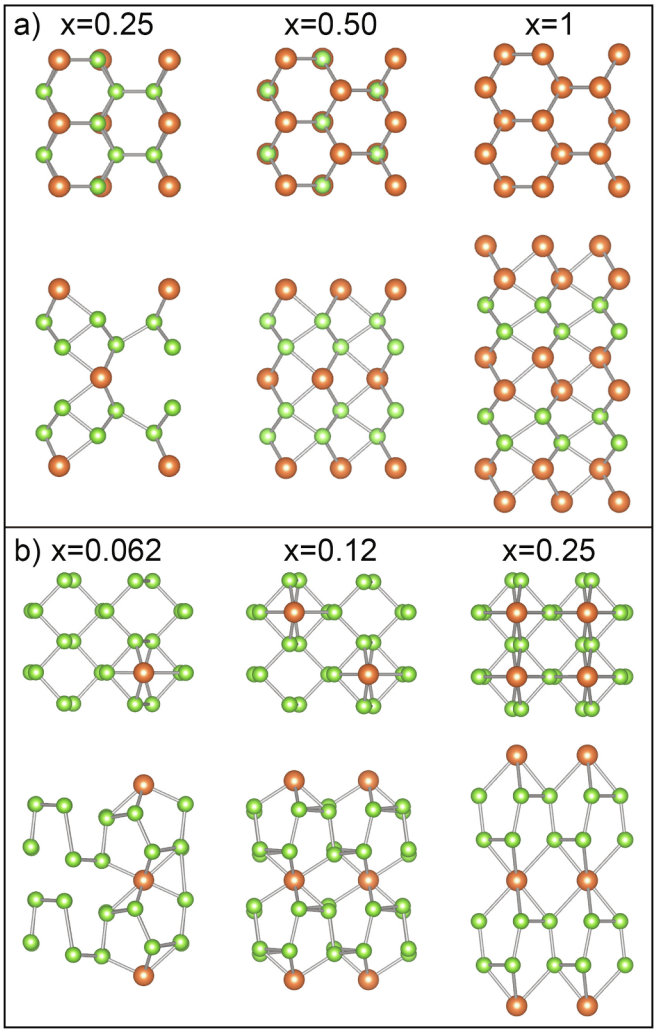

Fig. 6. The optimized structures of M-doped (a) ML-*hb*-As and (b) ML-*sw*-As, for varying M concentrations (M_xAs).

1.50 and 0.87 eV for ML-*hb*-As and ML-*sw*-As, respectively. Even ΔE for ML-*sw*-As is significantly smaller than that of ML-*hb*-As, it is still very high for room temperature diffusion, indicating the difficulty of intercalating M atoms. Accordingly, the intercalation (also leakage) can only occur through the vacancies or edges of the material.

The optimized structures of M_xAs for both phases are shown in Fig. 6. The ordered configurations are obtained up to $x = 1$ for ML-*hb*-As, and $x = 0.25$ for *sw*-As. M atoms are initially placed on V- and H-sites, which are found to be the most favorable adsorption sites for SL cases. The corresponding $E_b(M)$ and E_f energies are given in Table 3. $E_b(M)$ are higher than those for SL cases and also E_a, but follow a similar trend. The increase in $E_b(M)$ is partly due to the structural deformation as discussed above. Similar to SL case, E_f decrease with increasing x and they are smaller than those of pristine arsenene phases (3.29 eV) for all the concentrations. Variation of E_f implies that ML-M_xAs is becoming less stable with increasing cation content. It should be noted that, once the ordered pattern constraint is imposed, C decreases in ML-M_xAs when compared to SL configurations.

Prior to estimation of V_M, AIMD calculations are performed for ML-*hb*-As to obtain lower energy configurations. Similar to SL cases, crystalline to amorphous phase transition is noticed at ambient temperature. V_M, which are calculated with respect to the lower energy configurations, are shown in Fig. 7. The maximum of V_M is calculated as 0.92, 0.65, and 0.98 V for Li, Na, and K, respectively, reaching $C = 358$ mAhg^{-1} and the obtained results are comparable with the

Table 3
The average binding energies calculated with respect to single alkali atom (E_b) or bulk alkali metal (E_b') and the average bonding distance between alkali atom (M) and arsenene (d_{As-M}) for ML-*hb*-As and ML-*sw*-As with varying M concentrations (M_xAs).

Phase	M	x	E_b (eV)	E_b' (eV)	E_f (eV)	d_{As-M}(Å)
hb-As	Li	0.25	2.14	0.36	3.06	2.75
		0.50	2.34	0.57	2.90	2.75
		1.00	2.01	0.23	2.65	2.60
	Na	0.25	1.54	0.31	2.94	3.06
		0.50	1.73	0.50	2.77	3.05
		1.00	1.46	0.22	2.38	3.09
	K	0.25	1.41	0.46	2.92	3.35
		0.50	1.60	0.66	2.73	3.50
		1.00	1.10	0.16	2.20	3.48
sw-As	Li	0.062	2.29	0.69	3.30	2.47
		0.12	2.44	0.84	3.26	2.52
		0.25	2.58	0.98	3.21	2.57
	Na	0.062	1.13	0.04	3.23	2.73
		0.12	1.59	0.50	3.16	2.90
		0.25	1.84	0.76	3.06	2.97
	K	0.062	1.41	-0.69	3.17	3.06
		0.12	1.33	0.46	3.13	3.30
		0.25	1.68	0.81	3.02	3.34

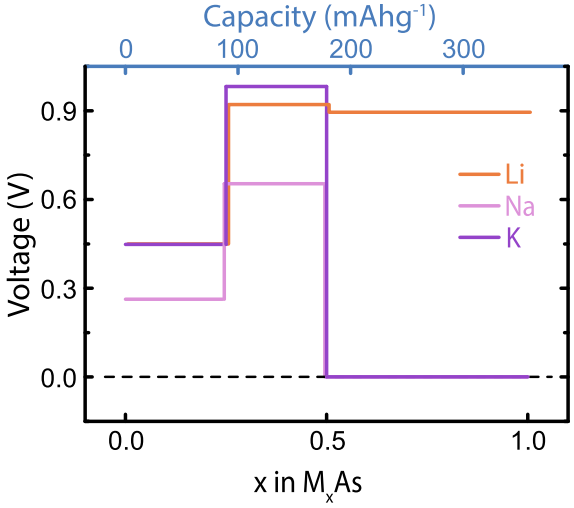

Fig. 7. Average open circuit voltages for ML-*hb*-As coated with alkali metals (Li, Na, and K) for varying concentration (M_xAs). The optimized (amorphous) structures are obtained with *ab initio* molecular dynamics calculations performed at ambient temperature.

experimental data [43]. The V_M increase up to $x = 0.5$ and then start to decrease and follow a similar trend to the SL cases. For ML-M_xAs, while V_M is higher than that of SL-M_xAs, C falls by half but still suitable for low charging voltage applications.

4. Conclusion

In summary, we performed first-principles calculations to reveal the interaction of alkali metal atoms (M: Li, Na, and K) with SL and ML (periodic) structures of *hb*-As and *sw*-As phases. Adatom adsorption analyses imply that M-atoms strongly bind to arsenene surface with adsorption energy range of 1.3–1.8 eV. The strong adatom-electrode binding suggests that the migration of ions from the cathode to the anode should be more favorable, thus it helps to alleviate the shuttle effect and enhance the cycling stability of the battery. The lateral diffusion energy barriers on arsenene are calculated to be low with the order of Li > Na > K and indicate fast diffusion for all ions. The structures are doped with varying M-concentration (M_xAs) and ordered patterns are obtained up to $x = 2$ for SL and $x = 1$ for ML systems. The theoretical storage capacity of *hb*-As is found to be higher than that of *sw*-As. On the other hand, deviations in ordered patterns and the decrease in formation energy with increasing doping level point out a possible structural transformation. The AIMD calculations indeed reveal that crystalline to amorphous phase transition occurs even for low concentrations level at ambient temperature. The corresponding (average) open-circuit voltages are found to be 0.68–0.88 V (0.65–0.98 V) with specific capacity up to 715 mAhg^{-1} (358 mAhg^{-1}) for SL (ML) configurations. Overall, non-crystalline phases are energetically more favorable than crystalline configurations and they provide more coherent results when compared with experimental data. The obtained voltage profile together with low diffusion barriers and strong metal-electrode binding suggests arsenene as a promising anode material to be used in for alkali-ion battery applications.

CRediT authorship contribution statement

Muammer Kanli: Formal analysis, Investigation, Writing - original draft, Writing - review & editing. **Mustafa Kurban:** Formal analysis, Investigation, Writing - original draft, Writing - review & editing. **Burak Ozdemir:** Formal analysis, Investigation, Writing - original draft, Writing - review & editing. **Abdullatif Onen:** Formal analysis, Investigation, Writing - original draft, Writing - review & editing. **Engin Durgun:** Formal analysis, Investigation, Writing - original draft, Writing - review & editing, Funding acquisition, Supervision.

Declaration of Competing Interest

The authors declare that they have no known competing financial interests or personal relationships that could have appeared to influence the work reported in this paper.

Acknowledgement

The calculations were performed at TUBITAK ULAKBIM, High Performance and Grid Computing Center (TR-Grid e-Infrastructure) and the National Center for High Performance Computing of Turkey (UHeM) under grant no. 5007092019. This work was supported by the Scientific and Technological Research Council of Turkey (TUBITAK) under Project No 117F241.

Appendix A. Supplementary data

Supplementary data associated with this article can be found, in the online version, at https://doi.org/10.1016/j.commatsci.2020.110000.

References

[1] H. Liu, A.T. Neal, Z. Zhu, Z. Luo, X. Xu, D. Tománek, P.D. Ye, ACS Nano 8 (2014) 4033.
[2] F. Xia, H. Wang, Y. Jia, Nat. Commun. 5 (2014) 1.
[3] L. Li, Y. Yu, G.J. Ye, Q. Ge, X. Ou, H. Wu, D. Feng, X.H. Chen, Y. Zhang, Nat. Nanotech. 9 (2014) 372.
[4] F. Ersan, D. Keçik, V. Özçelik, Y. Kadioglu, O.Ü. Aktürk, E. Durgun, E. Aktürk, S. Ciraci, Appl. Phys. Rev. 6 (2019) 021308.
[5] Y. Harada, M. Yamamoto, T. Baba, T. Kita, Appl. Phys. Lett. 104 (2014) 041907.
[6] H.-S. Tsai, S.-W. Wang, C.-H. Hsiao, C.-W. Chen, H. Ouyang, Y.-L. Chueh, H.-C. Kuo, J.-H. Liang, Chem. Mater. 28 (2016) 425.
[7] J. Ji, X. Song, J. Liu, Z. Yan, C. Huo, S. Zhang, M. Su, L. Liao, W. Wang, Z. Ni, et al., Nat. Commun. 7 (2016) 1.
[8] F. Reis, G. Li, L. Dudy, M. Bauernfeind, S. Glass, W. Hanke, R. Thomale, J. Schäfer, R. Claessen, Science 357 (2017) 287.
[9] V.O. Özcelik, O.Ü. Aktürk, E. Durgun, S. Ciraci, Phys. Rev. B 92 (2015) 125420.
[10] Y. Zhang, J. Lee, W.-L. Wang, D.-X. Yao, Comput. Mater. Sci. 110 (2015) 109.
[11] J. Lee, W.-C. Tian, W.-L. Wang, D.-X. Yao, Sci. Rep. 5 (2015) 11512.
[12] S. Zhang, Z. Yan, Y. Li, Z. Chen, H. Zeng, Angew. Chem. Int. Ed. 54 (2015) 3112.
[13] C. Kamal, M. Ezawa, Phys. Rev. B 91 (2015) 085423.
[14] E. Aktürk, O.Ü. Aktürk, S. Ciraci, Phys. Rev. B 94 (2016) 014115.
[15] J. Su, T. Duan, W. Li, B. Xiao, G. Zhou, Y. Pei, X. Wang, Appl. Surf. Sci. 462 (2018) 270.
[16] W. Tian, S. Zhang, C. Huo, D. Zhu, Q. Li, L. Wang, X. Ren, L. Xie, S. Guo, P.K. Chu, et al., ACS Nano 12 (2018) 1887.
[17] W. Jin, Z. Wang, Y.Q. Fu, J. Mater. Sci. 51 (2016) 7355.
[18] V.V. Kulish, O.I. Malyi, C. Persson, P. Wu, Phys. Chem. Chem. Phys. 17 (2015) 13921.
[19] W. Li, Y. Yang, G. Zhang, Y.-W. Zhang, Nano Lett. 15 (2015) 1691.
[20] K.-X. Chen, S.-S. Lyu, X.-M. Wang, Y.-X. Fu, Y. Heng, D.-C. Mo, J. Phys. Chem. C 121 (2017) 13035.
[21] J. Dai, X.C. Zeng, J. Phys. Chem. Lett. 5 (2014) 1289.
[22] O.U. Akturk, E. Akturk, S. Ciraci, Phys. Rev. B 93 (2016) 035450.
[23] F. Ersan, E. Akturk, S. Ciraci, J. Phys. Chem. C 120 (2016) 14345.
[24] G. Li, Y. Zhao, S. Zeng, J. Ni, Appl. Surf. Sci. 390 (2016) 60.
[25] K. Persson, V.A. Sethuraman, L.J. Hardwick, Y. Hinuma, Y.S. Meng, A. Van Der Ven, V. Srinivasan, R. Kostecki, G. Ceder, J. Phys. Chem. Lett. 1 (2010) 1176.
[26] F. Valencia, A.H. Romero, F. Ancilotto, P.L. Silvestrelli, J. Phys. Chem. B 110 (2006) 14832.
[27] F. Ersan, G. Gokoglu, E. Akturk, J. Phys. Chem. C 119 (2015) 28648.
[28] X. Zhang, S. Li, J. Li, M. Ye, Z. Song, S. Jin, B. Shi, Y. Pan, J. Yan, Y. Wang, et al., Comput. Condens. Matter 21 (2019) e00404.
[29] K.T. Chan, J. Neaton, M.L. Cohen, Phys. Rev. B 77 (2008) 235430.
[30] Y. Liu, B.V. Merinov, W.A. Goddard, Proc. Natl. Acad. Sci. U. S. A. 113 (2016) 3735.
[31] K. Persson, Y. Hinuma, Y.S. Meng, A. Van der Ven, G. Ceder, Phys. Rev. B 82 (2010) 125416.
[32] A. Sengupta, T. Frauenheim, Mater. Today, Energy 5 (2017) 347.
[33] J. Wan, Y. Xu, B. Ozdemir, L. Xu, A.B. Sushkov, Z. Yang, B. Yang, D. Drew, V. Barone, L. Hu, ACS Nano 11 (2017) 788.
[34] J. Zhao, Z.-H. Qi, Y. Xu, J. Dai, X.C. Zeng, W. Guo, J. Ma, Wiley Interdiscip. Rev. Comput. Mol. Sci. 9 (2019) e1387.
[35] J. Sun, H.-W. Lee, M. Pasta, H. Yuan, G. Zheng, Y. Sun, Y. Li, Y. Cui, Nat. Nanotech. 10 (2015) 980.
[36] E. Yoo, J. Kim, E. Hosono, H.-S. Zhou, T. Kudo, I. Honma, Nano Lett. 8 (2008) 2277.
[37] X. Li, H. Zhu, J. Materiomics 1 (2015) 33.
[38] Q. Sun, Y. Dai, Y. Ma, T. Jing, W. Wei, B. Huang, J. Phys. Chem. Lett. 7 (2016) 937.
[39] M. Akhtar, G. Anderson, R. Zhao, A. Alruqi, J.E. Mroczkowska, G. Sumanasekera, J.B. Jasinski, npj 2D Mater Appl. 1 (2017) 5.
[40] J. Zhou, Q. Sun, Q. Wang, P. Jena, Phys. Rev. B 90 (2014) 205427.
[41] Q. Zhou, W. Ju, Y. Yong, X. Li, J. Magnet. Magnet. Mater. 491 (2019) 165613.
[42] Q. Zhou, W. Ju, Y. Liu, J. Li, Q. Zhang, Appl. Surf. Sci. 506 (2020) 144936.
[43] Y.R. Lim, F. Shojaei, K. Park, C.S. Jung, J. Park, W.I. Cho, H.S. Kang, Nanoscale 10 (2018) 7047.
[44] H. Benzidi, M. Lakhal, M. Garara, M. Abdellaoui, A. Benyoussef, O. Mounkachi, et al., PCCP 21 (2019) 19951.
[45] B. Akgenc, J. Mater. Sci. 54 (2019) 9543.
[46] G. Kresse, J. Hafner, Phys. Rev. B 47 (1993) 558.
[47] G. Kresse, J. Hafner, Phys. Rev. B 49 (1994) 14251.
[48] G. Kresse, J. Furthmüller, Comput. Mater. Sci. 6 (1996) 15.
[49] G. Kresse, J. Furthmüller, Phys. Rev. B 54 (1996) 11169.
[50] P.E. Blöchl, Phys. Rev. B 50 (1994) 17953.
[51] G. Kresse, D. Joubert, Phys. Rev. B 59 (1999) 1758.
[52] J.P. Perdew, K. Burke, M. Ernzerhof, Phys. Rev. B 77 (1996) 3865.
[53] S. Grimme, J. Antony, S. Ehrlich, H. Krieg, J. Chem. Phys. 132 (2010) 154104.
[54] S. Grimme, S. Ehrlich, L. Goerigk, J. Comput. Chem. 32 (2011) 1456.
[55] H.J. Monkhorst, J.D. Pack, Phys. Rev. B 13 (1976) 5188.
[56] G. Henkelman, B.P. Uberuaga, H. Jónsson, J. Chem Phys. 113 (2000) 9901.
[57] G. Henkelman, H. Jónsson, J. Chem Phys. 113 (2000) 9978.
[58] M. Aydinol, A. Kohan, G. Ceder, J. Power Sources 68 (1997) 664.
[59] D. Kecik, E. Durgun, S. Ciraci, Phys. Rev. B 94 (2016) 205409.
[60] Y. Liu, V.I. Artyukhov, M. Liu, A.R. Harutyunyan, B.I. Yakobson, J. Phys. Chem. Lett. 4 (2013) 1737.
[61] L. Shi, T. Zhao, J. Mater. Chem. A 5 (2017) 3735.
[62] G.-C. Guo, D. Wang, X.-L. Wei, Q. Zhang, H. Liu, W.-M. Lau, L.-M. Liu, J. Phys. Chem. Lett. 6 (2015) 5002.
[63] S. Zhao, W. Kang, J. Xue, J. Mater. Chem. A 2 (2014) 19046.
[64] A. Nie, Y. Cheng, S. Ning, T. Foroozan, P. Yasaei, W. Li, B. Song, Y. Yuan, L. Chen, A. Salehi-Khojin, F. Mashayek, R. Shahbazian-Yassar, Nano Lett. 16 (2016) 2240.
[65] B. Mortazavi, A. Dianat, G. Cuniberti, T. Rabczuk, Electrochim. Acta 213 (2016) 865.
[66] Y. Jing, Z. Zhou, C.R. Cabrera, Z. Chen, J. Phys. Chem. C 117 (2013) 25409.
[67] C. Uthaisar, V. Barone, Nano Lett. 10 (2010) 2838.
[68] W. Zhang, Y. Liu, Z. Guo, Sci. Adv. 5, eaav7412 (2019b).
[69] S. Mukherjee, L. Kavalsky, C.V. Singh, A.C.S. Appl, Mater. Interf,. 10 (2018) 8630.
[70] See Supplemental Material for electronic band structure results.
[71] W. Luo, J. Wan, B. Ozdemir, W. Bao, Y. Chen, J. Dai, H. Lin, Y. Xu, F. Gu, V. Barone, et al., Nano Lett. 15 (2015) 7671.
[72] R.P. Joshi, B. Ozdemir, V. Barone, J.E. Peralta, J. Phys. Chem. Lett. 6 (2015) 2728.
[73] Z. Yang, D. Choi, S. Kerisit, K.M. Rosso, D. Wang, J. Zhang, G. Graff, J. Liu, J. Power Sources 192 (2009) 588.
[74] M. Mortazavi, C. Wang, J. Deng, V.B. Shenoy, N.V. Medhekar, J. Power Sources 268 (2014) 279.
[75] D. Cakir, C. Sevik, O. Gulseren, F.M. Peeters, J. Mater. Chem. A 4 (2016) 6029.